Photoelectrochemical CO_2 Reduction Devices Employing A Boundary Layer Flow for Direct Ocean Carbon Capture and Conversion

Shu Hu

shu.hu@yale.edu

Yale University

Bin Liu

Zheng Qian

Yale University

Xiang Shi

Yale University

Haoqing Su

Yale University

Yuze Zheng

Yale University

Chengxing He

Yale University

Rito Yanagi

Yale University

Wentao Zhang

Yale University

Atsu Kludze

Yale University

Article

Keywords:

Posted Date: February 12th, 2024

DOI: https://doi.org/10.21203/rs.3.rs-3921865/v1

Additional Declarations: There is **NO** Competing Interest.

Abstract

The capture and utilization of the dissolved inorganic carbon in seawater, e.g., bicarbonates, is a promising strategy for accessing fuels on demand and anywhere. We report unbiased photoelectrochemical (PEC) CO_2 reduction (CO_2R) devices, which can facilitate sustainable sunlight-to-syngas conversion. However, there have been very few reports on the use of dissolved inorganic carbon for direct light-driven CO_2 conversion to produce solar fuels. In this work, we design and implement 3D-printed PEC devices that employ a boundary layer flow. The flow over photoanode-photocathode pairs facilitates the efficient transport of in-situ generated CO_2(aq), which is produced upstream at $BiVO_4$ photoanodes, to downstream CO_2R Si photocathodes. In flowing seawater, the solar-to-fuels (STF) efficiency improved from 0.4–0.71%, a record for PEC CO_2R devices compared with $BiVO_4$-Si systems operating in static bicarbonate electrolytes with continuous CO_2 purging. Even in 2.3-mM HCO_3^- seawater, CO selectivity significantly increased from 3–21% with flow. The boundary layer flow confines the in-situ generated CO_2(aq) to the surface of $BiVO_4$ and Si photocathodes. Thus, an optimized flow field can increase the CO_2(aq) and proton transport flux and simultaneously reduce the CO_2(aq) residence time for its efficient utilization at Si photocathodes. Our process also features a high carbon efficiency: ~ 1 mmol CO_2 is additionally released per 4 mmol CO produced.

Introduction

Carbon capture, utilization, and storage (CCUS) technology is crucial to managing the ever-increasing anthropogenic carbon dioxide (CO_2) emissions. CO_2 is constantly emitted into the atmosphere from transportation sectors and from point sources and flue gases originating from processes such as fermentation, cement manufacturing, or natural gas combustion.[1] The atmospheric concentration of CO_2 is relatively low, currently at ~ 420 ppm, making direct air capture processes energy-intensive and costly. In contrast, there is an exchange of CO_2 between the atmosphere and the surface of the seawater, with a flux of ~ 0.4 Gt CO_2 per year[2,3]. The air-seawater equilibrium, along with the presence of alkaline species like Mg^{2+}, Ca^{2+}, HCO_3^-, and OH^-, results in seawater at a pH of 8.3[4,5]. Bicarbonates (HCO_3^-) are the primary form of dissolved inorganic carbon (DIC) in seawater, with a concentration of 2.3 mM, ~ 140 times higher in carbon molarity than atmospheric CO_2[6]. Thus, capturing and converting the 2.3 mM HCO_3^- in seawater, using solar energy, emerges as an economically feasible alternative to the direct air capture of CO_2.

Photoelectrochemical (PEC) devices harness sunlight to directly convert water and CO_2 into fuels. These devices employ photoanodes and photocathodes designed to drive water oxidation and CO_2 reduction (CO2R) reactions without needing an electrical bias [7–9]. Typically, the anodes and cathodes are arranged in a tandem configuration, with the anode-cathode pairs arranged back-to-back[10,11]. Tandem photoabsorbers allow for the effective utilization of the solar spectrum, optimizing light absorption. This

configuration ensures that the incident light that strikes the top of the photoanode also reaches the bottom photocathode, facilitating the generation of electrons and holes.

The operational photocurrent density per illumination area, $j_{photoelectrode}$, is determined by solar insolation, at ~ 1 kW/m^2 [12,13]. During water oxidation and CO_2R reactions, protons are produced at the anode and consumed at the cathode. For ion transport, protons (H^+ and H_3O^+, referred to as H^+ for simplicity) generated from anodic sites are transported to the back-to-back cathodic sites for consumption. For electrical conduction, photoanode and photocathode materials form ohmic contacts. The interfacial photocurrents at each electrode match the operational ionic current in PEC devices. The Eq. (1) below explains this relationship:

$$\iint j_{photoelectrode} dA = i_{ioniccurrent}$$

, where the total ionic current $i_{ioniccurrent}$ is equal to the total current flowing in between the electrically wired photoanode and photocathode, integrated over the surface area of photoelectrode *A*. During operation, the electrochemical potential drop due to ionic currents across the PEC device and the photocurrent are interdependent. Specifically, the potential drop due to ionic transport losses is due to electrolyte resistance, pH gradients, and concentration overpotentials of reactants and products (excluding protons). Kinetics losses at the cathodes and anodes also contribute to the total photocurrent loss in a PEC device in addition to transport losses[14–16].

Seawater, with its ionic strength of ~ 0.7 M, is a good ionic conductor[17,18]. Consequently, photocurrent losses in PEC CO_2R devices primarily stem from 1) kinetic losses associated with water oxidation and CO_2R, 2) the presence of a pH gradient, and 3) the presence of concentration overpotentials pertain to the difference at cathodes and in bulk electrolytes, such as the concentration of dissolved CO_2, i.e., [CO_2(aq)]. Recent studies on unbiased CO_2R have reported solar-to-fuel (STF) conversion efficiencies of 0.08%[19], 0.43%[20], 0.63%[21], and 0.7%[22]. In those reported PEC devices, proton transport from the anode to the back-to-back arranged cathode via diffusion [19,20]. As the protons diffuse in buffered electrolyte solutions, they interact with the buffer anions and subsequently generate an ionic current driven by the transport of major mineral species, i.e., Na^+, Cl^-, Mg^{2+}, and Ca^2. This creates a pH gradient, leading to a higher pH at the cathode and reducing local [CO_2(aq)]. PEC devices previously reported have been evaluated by bubbling CO_2 gas in bicarbonate solutions at pH ~ 7, saturating the bulk electrolyte with CO_2(aq). In static electrolytes, CO_2 produced through acidification can only reach the cathode through diffusion. As CO_2(aq) diffuses towards the cathode, it gets consumed in acid-base reactions such as $CO_2 + OH^- \rightarrow HCO_3^-$. Even with continuous CO_2 bubbling, [CO_2(aq)] at the cathode during operation is very low, limiting the CO_2R partial current. Moreover, feeding gaseous CO_2 for sunlight-driven CO_2 conversion over a large area may not be practical. Thus far, reported PEC devices that leverage flowing electrolytes without CO_2 bubbling remain largely unexplored.

Implementing engineering design approaches such as flowing seawater in PEC devices presents several opportunities for improving the efficiency of direct ocean capture and conversion. We present a 3D-printed photo reactor, designed for the unbiased PEC capture and in-situ conversion of CO_2 from dissolved bicarbonates in flowing seawater. This reactor is comprised of a $BiVO_4$ photoanode for generating CO_2(aq) from seawater in real-time and a Si photocathode for its subsequent reduction into fuels. We couple solar-driven CO_2 conversion with CO_2(aq) transport, where the primary mode of transport is convection. In this device, the ionic current flows upstream to downstream while the electric current runs between the back-to-back photoanodes and photocathodes. This configuration can be periodically repeated to achieve scaled-up, solar-driven, direct ocean CO_2 conversion.

The flow of seawater is expected to improve electrolyte conductivity and reduce ion conductivity losses. The benefit of flowing seawater will be quantified in a stepwise fashion through combined *in-situ* fluorescence spectroscopy and multi-physics modeling. Our designs are informed by finite element modeling and simulations and allow for precise control over local pH, [CO_2(aq)], and CO_2(aq) flux. Controlling the interactions of CO_2(aq) and (bi-)carbonate species is critical in CO_2R reactions[23,24]. Adjusting the local pH at the photoanodes to ≤ 6 sufficiently leads to the conversion of dissolved bicarbonate and carbonate into CO_2[25]. Besides, the flow replaces the H^+ diffusional transport with the H^+ convective transport, which is expected to significantly reduce the pH gradient from the anode to the cathode. Thus, more CO_2(aq) is made available at the cathodes by minimizing the pH difference and reducing transport time.

Well-defined convective flow over the planar surfaces of upstream photoanodes and downstream photocathodes, known as Poiseuille's flow or a boundary layer flow, is also expected to confine the generated protons near the photoanode surface. This flow limits the seawater acidification process to the photoanode's surface, thus allowing for effective delivery of in-situ generated CO_2(aq) to the cathodic CO_2R active sites. We hypothesize that CO_2(aq), generated by photoanodic acidification can live long enough in the CO_2R photocathode's locally alkaline environment. Thus, well-defined convective flow reduces the residence time of the CO_2(aq) within the photocathodes' local alkaline environment. Compared to static electrolyte systems, the proton flow approach is expected to co-optimize both solar-to-fuel conversion efficiency and CO_2R selectivity. Eventually, we match sunlight-driven photocurrent flux with CO_2 transport flux in a flow of locally acidified seawater containing only 2.3-mM HCO_3^-.

Results and discussion

Design and construction of seawater flow reactor for CO_2 capture and in-situ conversion

Simulated seawater was prepared by dissolving 35.5 g of simulated seawater salt (Instant Ocean®, see table S1 for detailed chemical compositions) in 1 L 18 mega ohm deionized water. The chemical composition of this simulated seawater solution was designed to simulate the chemical, electronic, and ionic properties of natural seawater (Table S1). Although Na^+ and Cl^- ions are the primary carriers of the

ionic current in this solution, it is essential for protons generated at the upstream photoanodes to be transported downstream photocathodes for consumption. To address these issues, we developed an original vortex reactor design and 3D-printed the flow reactor (Fig. 1a, photographs in Fig. S1a and S1b).

The 3D-printed vortex reactor design features a periodic array of photoanode-photocathode pairs, each configured back-to-back and aligned in parallel to each other. In each pair, a Si photocathode and a $BiVO_4$ photoanode are positioned back-to-back, maintaining a distance of 2 cm apart. The $BiVO_4$ photoanode is 2 cm in length and 1 cm in width, while the Si photocathode is 0.5 cm in length and 0.5 cm in width. Ag-Au/CrO_x catalysts are deposited on the Si photocathode for CO_2R (fabrication details in the Methods section). Each $BiVO_4$-Si pair is oriented at an angle towards the sun and arranged horizontally in parallel to optimize light capture. This design, where parallel pairs of photoelectrodes are utilized, can be indefinitely repeated for manufacturing scale-up. Electrical contacts are made between the back-to-back photoanode and photocathode pairs, while the ionic currents are between the upstream photoanode and the downstream photocathode. The seawater flow over each photoelectrode pair is identical.

Seawater flow was designed to sweep across the surface of $BiVO_4$ photoanode, carrying H^+, HCO_3^-, and CO_2(aq) from the photoanode surface to downstream photocathodes that facilitate CO_2(aq) capture and in-situ CO_2 reduction. The seawater flow field, confirmed through computational simulations, is characterized by laminar seawater flow across the $BiVO_4$ photoanode surface, which oxidizes seawater to O_2 (Fig. 1b). Consideration was also given to the time needed to generate CO_2(aq) and its limited lifetime when its concentration exceeded its equilibrium concentration in the bulk solution. To manage this, a vortex flow is created for CO_2(aq) to pass over Si photocathode surfaces (Fig. 1c) mounted and electrically wired to the back of a $BiVO_4$ photoanode (shown in supporting movie S1). This design enables the direct transport of the generated CO_2(aq) to the Si photocathode without hindering light absorption. Moreover, this flow tunes the residence time of CO_2(aq) on the surface of the Si photocathodes: an excess of CO_2(aq) can undergo subsequent reduction into valuable chemical products before it diffuses into the bulk seawater solution or reacts with alkaline species (OH^-, CO_3^{2-}) near the Si photocathode. Gas bubbles are continuously emitted from photoelectrode surfaces (Fig. 1d, see supporting movie S2), underscore the importance of well-defined convective flow for solar-driven ocean-based CO_2 capture and conversion.

The effect of proton convective transport on the photoelectrochemical CO_2 reduction rate and the overall solar-to-CO conversion efficiency was investigated by systematically varying the flow velocities during PEC device operation under AM 1.5G illumination (100 mW/cm^2). During the process of seawater oxidation at the $BiVO_4$ photoanodes, protons are generated in quantities exceeding their equilibrium concentration in the bulk seawater solution. This leads to a reduction in the local pH and drives the conversion of HCO_3^- to CO_2(aq) as it moves along the path of convective transport. The enhancement effects of convective proton flow were experimentally measured and then supplemented with analysis from numerical simulations.

In this study, flow rate was measured using the average volumetric rate at which seawater solution left the inlet nozzle, which was 0.3 cm away from the closest photoelectrode pair (Fig. S1c). To quantify the flow velocity, the volumetric flow rate was divided by the cross-sectional area of the tubing. The fuels produced in this system include CO and H_2 gases, with liquid products falling below the detection limit, as confirmed by nuclear magnetic resonance (NMR) spectroscopy (Fig. S29). Analysis of the gas product composition at a flow velocity of 0 m/s, revealed that the Faradaic efficiency for CO and H_2 are 3% and 97%, respectively. The low CO selectivity suggests that there is a preference for electrons to reduce of H^+ to form H_2 under static flow conditions, where [CO_2(aq)] is expected to be around 2-μmol. Increasing the flow velocity to 0.77 m/s, resulting in a CO Faradaic efficiency increase from 3–19%. This significant increase in CO production underscores the crucial role that flow plays in both the in-situ generation and mass transfer of CO_2(aq) from the upstream photoanode to the downstream Si photocathode for in-situ CO_2 conversion (Fig. 2a). Under static flow conditions, CO generation over a period of 4.5 hours was determined to be 2.97 μmol per cm^2 illumination area. However, CO generation over the same period significantly increased to 14 μmol/cm^2, when the flow velocity was increased to 0.77 m/s (Fig. 2c). Other flow velocities also increased the CO production rate and Faradaic efficiency, as shown in Fig. S2. The increase in CO production can be attributed to the elevated [CO_2(aq)] at the cathodic surfaces.

A similar trend was observed when measuring gaseous CO_2 generation (Fig. 2b). Under static flow conditions, CO_2 generation was determined to be 1.85 μmol per cm^2 illumination area over a period of 4.5 h. When the flow velocity was increased to 0.77 m/s (see other flow velocities shown in Fig. S2), the amount of CO_2 extracted over the same timeframe increased to 3.5 μmol/cm^2. Excess CO_2(aq) at the headspace-seawater interface may eventually be released as CO_2 gas. Correspondingly, the STF efficiencies increased from 0.4–0.71% with the increase in flow velocity. This level of performance serves as our benchmark STF for $BiVO_4$-based devices for unbiased CO_2R (Table S6). The STF efficiency reached a maximum at a flow velocity of 0.77 m/s (Fig. 2d). This increase in efficiency highlights the importance of convective flow in improving ionic transport and minimizing concentration overpotentials, which are in systems without flow. The observed increase in CO_2 generation supports our hypothesis that in-situ generated CO_2(aq) has a sufficient lifetime to participate in CO_2R downstream. To summarize, this $BiVO_4$/Si vortex reactor in seawater demonstrates the first instance of utilizing an unbiased PEC tandem device to simultaneously capture and convert utilize dissolved inorganic carbon in seawater.

Construction of $BiVO_4$ photoanode for extracting CO_2 from seawater

$BiVO_4$ was chosen to serve as the photoanode material for its ability to provide the high oxidation potential per charge transfer required for seawater oxidation. Thin-film $BiVO_4$ photoanodes (Fig. 3a) were fabricated on fluorine-doped tin oxide (FTO) glass via a metal-organic decomposition method (see Methods with the photograph in Fig. S3). The thickness of the $BiVO_4$ photoanode was approximately 200

nm (Fig. S4). X-ray diffraction (XRD) (Fig. S5) measurements were consistent with what has been previously observed in relevant studies[13,26]. Scanning electron microscopy (SEM) images (Fig. 3b) revealed the nanoporous morphology of the $BiVO_4$ photoanode, which can increase the photoanode's contact area with seawater, improve charge transfer efficiency, and induce surface pH variations. The presence of Bi and V was confirmed through SEM element mapping (Fig. 3c and 3d). To enhance oxygen evolution kinetics in seawater, $NiFe(OH)_x$ catalysts were deposited on the photoanode's surface by dip coating[27]. A thin CrO_x layer was then photodeposited onto the $NiFe(OH)_x$ catalysts to prevent chlorine oxidation and the subsequent corrosion of the $BiVO_4$ photoanodes in seawater.

The PEC oxygen evolution measurements were performed under AM 1.5G illumination (100 mW/cm^2) in seawater with a of pH 8.3 at ambient conditions. The $BiVO_4$ photoanode with $NiFe(OH)_x/CrO_x$ catalysts biased at 0.6 vs RHE exhibited the same onset potential of 0.2 V vs RHE but at a higher current density of 1.8 mA/cm^2 than the 0.5 mA/cm^2 without cocatalysts (Fig. 3e). The $NiFe(OH)_x$ catalyst increased the oxidation reaction's rate, allowing for applied bias photon-to-current efficiencies (ABPE) of 0.51% to be achieved (Fig. S6). $BiVO_4$ photoanodes with CrO_x exhibited the same onset potential and saturated current density (Fig. 3f), indicating that the thin CrO_x layer does not impede photogenerated hole charge transfer. Under AM 1.5G illumination, an O_2 Faradaic efficiency of 94.5% at 0.6 V vs RHE over a 2 h period was achieved, suggesting that the majority of the photogenerated holes were utilized for oxygen evolution, with significant oxygen bubble formation also observed (Fig. S7). Additionally, the $BiVO_4$ photoanode with $NiFe(OH)_x$ catalysts exhibited a robust photocurrent density after 10 h (Fig. 3g). The generation of hypochlorite (ClO^-) was negligible, as confirmed with hypochlorite detection.[28,29] Furthermore, the color of the seawater remained clear after 10 hours of operation (Fig. S8). The high O_2 FE and the excellent stability were attributed to the CrO_x layer, which may behave as a Lewis acid to effectively modulate the local reaction microenvironment of the $NiFe(OH)_x$'s water-oxidation sites to effectively prevent chloride attack[28,29].

pH map above photoelectrodes reveals spatial confinement effects of flowing seawater

The concentration of reactants is often used as a quantitative indicator for the limiting electrochemical currents. Applying this concept to our system, if diffusion were the predominate transport mechanism, bulk [CO_2(aq)] in seawater would act as our indicator for the CO_2(aq) flux, and consequently the CO_2R partial current. In this study, it is important to note that the convective flux of in-situ generated CO_2(aq) substantially contributes to the downstream CO_2R currents. Calculations reveal that the bulk seawater [CO_2(aq)] remains at the 0.11 mmol level near the Si photocathodes. In other words, the diffusive transport of mmol-level CO_2(aq) does not sufficiently account for the measured CO_2R partial current density of ~ 0.2 mA cm^{-2}. To elucidate the coupled processes of light-generated excess proton generation and acid-base reactive transport, we employed experimental pH mapping and numerical

calculations. We took this approach to quantify and visualize both the concentration and flux of CO_2(aq) that is otherwise difficult to measure.

To measure the pH spatial distribution in a seawater flow over the $BiVO_4$ photoanode surfaces, we developed an original in-situ photo-fluorescence technique using confocal fluorescence spectroscopy (Fig. 4a). Carboxy SNARF-1 was selected as the fluorescent pH indicator due to its emission spectrum exhibiting a pH-dependent wavelength shift. pH at a given point was measured by calculating the fluorescence intensity at two different emission wavelengths (580 and 650 nm)[30,31]. To mitigate the potential influence of illumination (415 nm laser) on the pH indicator dye's peak intensities and position, back-illumination was employed (photographs of the apparatus used in the pH measurement are shown in Fig. S9, and S10). The pH indicator was first calibrated using various standard solutions (Fig. S11). An immersion water lens (60 x) was used for high resolution spectra acquisition, and the Raman laser was focused on the top surface of $BiVO_4$ photoanodes (Fig. 4b and Fig. S12). Spatial mapping revealed uniform pH of ~ 8.3 across the entire $BiVO_4$ photoanode at open circuit potentials (Fig. 4c). This observation suggests that the introduction of flow confines the acidification process that the $BiVO_4$ photoanode surface uniformly generate H^+, whereas the pH of the seawater at > 100 µm above the photoanode surface plane remains identical to the inflow seawater pH. Each pH data point was determined from the pH-indicator emission spectra, with an emission peak at 650 nm indicating a pH value of ~ 8.35 (Fig. S11), which is consistent with the seawater's pH of 8.30 measured by a pH meter. When a 0.6 V vs RHE potential was applied to the $BiVO_4$ ohmic back contact, flowing seawater was oxidized at a current density of 0.5 mA/cm^2. Under these conditions, the near-surface fluorescence spectra revealed an increase at the 580 nm emission peak, indicating a decrease in pH during seawater oxidation (Fig. S13).

To illustrate the effect of flow velocities on spatial pH differences, we mapped spatial pH variations from 0–100 µm above the $BiVO_4$ photoanode surface during PEC seawater oxidation at a current density of 0.5 mA/cm^2. At a flow velocity of 0 m/s (Fig. 4d), protons generated by water oxidation diffuse from the $BiVO_4$ photoanode surface to the bulk solution, driven by a concentration gradient. Protons accumulate near $BiVO_4$ surface for ~ 5 minutes and diffuse outwards. The pH is lowered to ~ 4.3 at 0–100 µm above the $BiVO_4$ photoanode surface, indicating that the water oxidation reaction at the $BiVO_4$ photoanode surface significantly alters the local pH. When the flow velocity is increased to 0.16 m/s, pH mapping revealed four distinct regions colored blue, green, yellow, and red. Near the $BiVO_4$ photoanode surface was the blue region, corresponding to lower pH and attributed to the higher proton concentration at the photoanode surface (Fig. 4e). The random pH variation within the blue region (Fig. 4e and 4f) was attributed to random voids in $BiVO_4$ thin film's nanoporous structure (shown in Fig. 3d).

At 60-µm above the photoanode surface, there was a gradual increase in the pH, indicated by the yellow region that continued until it approached the red region. As the flow velocity increased from 0.16 to 0.77 m/s, there was a corresponding increase to red region's area on the pH maps (Fig. 4e – 4h). This suggests that convective flow serves to effectively confine generated protons to the photoanode surface,

to prevent their diffusion into the bulk seawater solution, and to enhance CO_2 extraction from seawater (Fig. S14). Modeling indicates that the downstream pH increases are due to proton consumption at the cathode. Furthermore, the pH variations downstream are significantly less under flow conditions than when there is no flow. The overall effect of convective flow is to reduce ionic conductivity, pH gradient, and CO_2(aq) concentration overpotential losses. Subsequent analysis will focus on the effects of the flow field on non-equilibrium CO_2(aq) transport flux, and the rate and selectivity of CO_2R at the photocathodes.

Modeling time-dependent CO_2(aq) convective-diffusive transport coupled with the non-equilibrium generation and neutralization of protons

We modeled our PEC reactor as a flatbed device, with an upstream photoanode and downstream photocathode arranged side-by-side. The modeling was conducted in 2D as the electrode behavior across the width dimension is uniform. Both the anode and cathode were 1 cm long and 2 cm apart at the bottom of the seawater chamber, with the electrolyte above the electrodes 1 mm in height (Fig. 5a). These dimensions match the dimensions of the 3D printed vortex reactor (Fig. 1a). Electrolyte flow velocity in our model was determined from our experimental data, with the chamber walls modeled with no-slip boundary conditions. To develop an understanding of the flow within our system, we first determined the flow field at varying velocities: 0.16 m/s, 0.34 m/s, 0.56 m/s, and 0.77 m/s. The resulting Reynolds numbers for these flow velocities were 320, 680, 1120, and 1540 respectively, all below 2000, confirming that our vortex reactor operates under laminar flow conditions.

The simulated PEC reaction was conducted in 2 mM HCO_3^- with pH 8.3. The H^+ and OH^- generation rates, alongside the CO_2(aq) consumption rate were based on the partial current density of CO_2R on the Si photocathode (Fig. 2d). This model only considers convective and diffusive transport across anode and cathode near the surface of electrodes and in the bulk solution, because the flux contribution from electric field-induced migration is negligible: the distance between the photoanode and photocathode is 2 cm; and in seawater, ions such as K^+, Na^+, Mg^{2+}, and Ca^{2+} drive the conductive ion flux. The model tracked the path of the protons generated at the photoanode as they transported toward the photocathode via convection and diffusion. During transport, the protons may encounter OH^-, HCO_3^-, and CO_3^{2-} ionic species. The flow field also allows for “in situ”-generated CO_2 to be transported to the cathodic sites for CO_2R. The concentration of a specific chemical species *i*, denoted as C_i,were calculated using multi-physics simulations. Equations (2) and (3) were used to describe the reactive transport of reactive species *i*, such as CO_2(aq), H^+, OH^-, HCO_3^-, and CO_3^{2-}:

$$\frac{\partial C_i}{\partial t} = -\nabla \bullet N_i + R_i$$

2

$$N_i = -D_i \nabla C_i + \mathrm{varvec}v C_i - \frac{Z_i F}{RT} D_i C_i \nabla \varphi$$

3

, where C_i represents the concentration of species *i*, N_i is the flux, $-\nabla \bullet N_i$ is the net influx (with the divergence of the flux is taken as a negative value), and R_i is the net rate of production from chemical reactions per unit time, D_i is the diffusion coefficient of species *i*, and $\mathrm{varvec}v$ represents the local velocity. The reactive transport of seawater DIC species (e.g., CO_2(aq), HCO_3^-, and CO_3^{2-}), protons, and hydroxides were analyzed to determine whether a species is being produced ($R_i > 0$) or consumed ($R_i < 0$) in a chemical reaction. Using R_{CO2} as an example, details of R_i for are provided in the supporting information. According to Eq. (3), the Nernst-Planck equation, N_i considers contributions from diffusion, convection, and a negligible migration flux. The boundary conditions, kinetic rate constants, diffusion coefficients, and electric charge of species are shown in Fig. S15b, tables S2 and S4.

A seawater flow confines photoanode-generated protons within boundary layers

The pH mapping at the $BiVO_4$ photoanodes revealed that varying the seawater flow velocity leads to significant changes in pH spatial distribution (Fig. 4e - f), and consequently affects [CO_2(aq)] generated through acidification. We employed an analytical model that considers the convection and diffusion of H^+ in a semi-quantitative manner to analyze the principle of flow-induced confinement of H^+ produced at the photoanode. We then utilized COMSOL Multiphysics to couple mass transfer with acid-base reactions. Our COMSOL model considered the diffusion of all chemical species dissolved in seawater, while accounting for the real-time acid-base speciation reactions of all dissolved carbon species. H^+ and OH^- were actively generated at the anodes and cathodes, respectively. The in-situ generation of CO_2(aq) and the measurement of the CO_2 flux are performed under non-equilibrium conditions.

In our analytical model, for simplicity, we start by assuming [H^+] in bulk seawater solution is zero. Drawing inspiration from Pohlhausen's integral approach to solve for boundary layer thickness, we proposed a linear concentration distribution for the CO_2 flux as a function of distance from electrode surfaces[32]. This approach, combined with a series of boundary conditions elaborated on later, allows us to estimate the boundary layer thickness. We theorize that at a given point along the x-axis, the concentration exhibits a linear distribution relative to the distance from the cathode, z, as described in Eq. (4). This linear distribution matches closely with the results obtained from COMSOL Multiphysics (Fig. S16). Within this framework, the boundary layer is defined as the envelope where $c > 0$, and the thickness of the boundary layer is denoted as $\delta(x)$.

$$c(x,z) = c_0(x)\left(1 - \frac{z}{\delta(x)}\right)$$

4

This model is constrained by two boundary conditions: proton generation and their transport by convection and diffusion. We assume a uniform generation rate of H^+ from seawater oxidation as described in Eq. (5). The number of protons flowing through the cross-section at x = x_0 is equal to the total number of protons generated at the anode at $x < x_0$, as stated in Eq. (6). Furthermore, the electrolyte flow between the two parallel plates conforms to Poiseuille flow, as described in Equations (7), where u_0, k, z, and d are the average flow velocity among the reactor, velocity gradient, the height above the anode, and thickness of the reactor, respectively.

$$-D\frac{\partial c}{\partial z}|_{z=0} = \frac{i}{F}$$

5

$$\int_0^{\delta(x)} c\left(x_0, z\right) u\left(z\right)\ \mathrm{d}z = \frac{i}{F} x_0$$

6

$$u\left(z\right) = 6u_0 \cdot \left(-\left(\frac{z}{d}\right)^2 + \frac{z}{d}\right) \approx kz \left(k = 6\frac{u_0}{d}\right)$$

7

Equations (4) to (7) are combined to solve the thicknesses of the H^+ boundary layer as a function of the flow velocity u_0 and flow distance x_0 (Fig. 5a).

$$\delta \approx \left(\frac{6Dx_0}{k}\right)^{\frac{1}{3}} = \left(\frac{x_0 Dd}{u_0}\right)^{\frac{1}{3}}$$

8

Equation (8) provides a semi-quantitative expression for calculating the thickness of the concentration boundary layer. As the flow velocity increases, the CO_2(aq) boundary layer thickness decreases (Fig. 5a) and the CO_2 flux produced by acidification becomes concentrated within the narrowed region. At the same flow velocity, the boundary layer downstream is thicker than upstream (Fig. 5a). This can be attributed to higher downstream CO_2(aq) and proton concentrations. At a fixed position in the x_0 direction (take x_0 = 0.8 cm as an example), the boundary layer thickness decreases from 77 μm at a flow velocity of 0.16 m/s to 40 μm at flow velocity of 0.77 m/s (Fig. 5a). This reduction is due to an increase in the convective mass transport flux in the z-direction as the velocity increases, resulting in a thinner boundary layer.

Quantitative analysis of CO_2(aq) transport flux to Si photocathodes

The COMSOL numerical model allows us to precisely define boundary layer thicknesses (definition shown in supplementary materials section). Our COMSOL model considers reversible CO_2-speciation reactions that can occur during transport. The dashed line in Fig. 5b shows the linear distribution assumption for CO_2(aq) flux, which is consistent with the linear flux-position relationship that exists outside the boundary layer according to our model calculation. This allows for our numerical model to be compared against our analytical boundary layer analysis: based on Eq. (8), the boundary layer thicknesses at x = 0.8 cm along the anode at flow velocities of 0.16, 0.34, 0.56, and 0.77 m/s are 80, 60, 50, and 40 μm, respectively (Fig. 4e - h). In comparison, the numerical boundary layer thickness at the same position and flow rates are 77, 60, 51, and 45 μm. Furthermore, the pH map contours match the quantitative flow boundary (see supplementary materials). These strong correlations not only indicate that the assumptions proposed during our numerical calculations are reasonable but also confirm the accuracy and applicability of in-situ spectroscopy for monitoring local pH during PEC water splitting and CO_2R.

Across all flow velocities, the observations made from our pH mapping using *in-situ* fluorescence measurements (Fig. 4e – 4h) closely matched the trends of the COMSOL-simulated boundary layers (Fig. 5a). This validates our model and allows us to visualize CO_2(aq) generation, transport flux, and consumption behavior, along the photoanode-photocathode flow path. The cross-section located 1 cm from the anode's far end (x = 1) was taken to illustrate the distribution of CO_2(aq) flux (Fig. 5b). At this specific cross-section, CO_2(aq) flux peaks within a 40-μm range from the photoelectrode surface in the z-direction. The peaking of the CO_2(aq) flux was observed at all flow velocities. As the flow velocity increased from 0.16 to 0.77 m/s, the CO_2(aq) flux increased from 11.7 to 18.8 $mmol \cdot m^{-2} \cdot s^{-1}$, demonstrating the ability of the flow field to enhance the CO_2(aq) flux. The CO_2(aq) flux is primarily driven by convective mass transfer. CO_2(aq) generated through acidification was concentrated within a specific height range, closely matching what was determined with our semi-quantitative model. During CO_2(aq) transport at flow velocities of 0.77 and 0.16 m/s from the anode to the cathode, the CO_2(aq) fluxes at the front end of the cathode were 13.53 and 7.5 $mmol \cdot m^{-2} \cdot s^{-1}$ were achieved respectively (Fig. S20). This indicates that higher flow velocities correspond to higher CO_2(aq) flux near the cathode surface, which is consistent with our findings that the CO_2 selectivity and STF efficiency increased at higher flow velocities (Fig. 2a). Moreover, the vector profile of CO_2(aq) flux at 0.77 m/s provides an overview of CO_2 generation, transportation, and conversion (Fig. 5c). The arrows indicate a downward CO_2(aq) flux on the cathode surface, indicating the presence of diffusive mass transfer when CO_2(aq) is transported to the cathode surface (other flow rates shown in Fig. S21), driven by the CO_2R reaction occurring on the cathode surface that lowers the local CO_2 concentration. As a result, downward diffusion contributes to CO_2(aq) transport within the boundary layer.

Chemical-species confinement via a boundary layer flow allows photoanodes to generate CO_2(aq) flux effectively

By applying a seawater flow, the H^+ produced at the anode and the CO_2(aq) generated from these H^+ can be confined within the boundary layer. We further experimentally benchmarked the effect of CO_2 compensation on CO_2R Faradaic efficiency using a model flat-plate flow reactor. Electrocatalytic electrodes are side-by-side in a flow-by configuration. Instead of photoelectrodes, we have the opportunity to arbitrarily turn on and turn off proton generation upstream.

An Ag-Au/CrO_x cathode and an FTO/NiFe$(OH)_x$/CrO_x anode were employed (fabrication details in the Methods), and the catalysts used are the same as photoelectrodes. To compare the current density and selectivity of cathodes with and without acidification effects from upstream anodes, the terminology used is as follows: “with CO_2 compensation” means that the anode was placed side-by-side with the cathode within the same reactor, while “without CO_2 compensation” indicates that the anode was situated outside the cell, separate from the cathode. The flow rate-dependent chronoamperometry data reveals that under static conditions, both with and without CO_2 compensation configurations exhibit comparable current densities (Fig. 5d). However, as the experiment progresses, the current densities steadily decline. This trend suggests an insufficient mass transfer of reactants, i.e., H^+ and CO_2, to adequately sustain the reductive current. The scenario takes a different turn when introducing the flow into the cell. In this case, the current densities remain stable and exhibit an increase with the ascending flow rate within the range of 0 to 0.77 m/s, implying that the mass transfer is enhanced. Notably, the reductive current densities observed with adjacent anodes (with CO_2 compensation) are greater than those observed when no acidifying CO_2 is transferred to the cathode (without CO_2 compensation). This promotion in current can be attributed to the elevated CO_2 concentration on the cathode surface in our configuration. The gas composition analysis indicates that, under a flow rate of 0 m/s, the faradaic efficiency for CO and H_2 is 3% and 97%, respectively, which suggests that electrons primarily favor the reduction of H^+ to form H_2 under these conditions. The CO Faradaic efficiency increases from 3–21% as the flow rate rises, highlighting the crucial role played by mass transfer and CO_2 compensation for CO_2 in-situ conversion (Fig. 5e). The partial current for CO production increases proportionally with the flow rate, providing further evidence that the precisely controlled seawater flow serves to accelerate both the overall reaction rate (current density) and enhance CO selectivity (Fig. 5f). Figure 5e shows a higher CO_2R FE than Fig. 5f. The flat plate reactor (Fig. 5e and 5f) and vortex flow reactor (Fig. 2b – 2d) exhibit comparable CO_2R performance, indicating that vortex flow can effectively enhance convective mass transfer to confine the CO_2 in the boundary.

Conclusion and Outlook

In summary, this work reports an original 3D-printed photoelectrochemical solar fuel production device designed with a well-defined flow field for CO_2 capture and in-situ conversion using seawater and sunlight as the only inputs. Specifically, the optimized seawater flow is designed to pass over the $BiVO_4$ photoanodes surface, carrying H^+ and CO_2(aq) to reach the surface of the Si photocathodes where the

CO_2 reduction reaction occurs. For solar-driven unbiased CO_2 reduction in seawater, the CO Faradaic efficiency exhibits a notable improvement, increasing significantly from 3% at a flow rate of 0 m/s to 21% at a laminar flow rate of 0.77 m/s. These critical enhancements point out the important role of managing H^+ mass transfer and CO_2(aq) flux supplied to CO_2R cathodes in unbiased PEC solar fuel production. The reactor developed in this study bridges the gap between single-component systems (such as artificial leaf structures) and device-level configurations.

The role of the flow field is to confine the CO_2 generated at the anode within the boundary layer. A higher flow rate corresponds to a thinner boundary layer. While the total CO_2 production remains constant, this leads to an increased CO_2 flux near the electrode surface. This facilitates an effective constraint of CO_2(aq) near the cathode surface and benefits the back diffusion of CO_2(aq) within the boundary back to the cathode surface, which has a lower CO_2 concentration than everywhere else. Consequently, it enhances the selectivity of the cathodic CO_2R. A similar approach is to use electrolytic cation exchange modules and bipolar membrane electrodialysis[6,33]. Both approaches have recently been reported to innovatively extract CO_2 from carbonate solution by using protons produced from anodic reactions. However, this process may be limited by the high energy consumption due to water dissociation in addition to the energy input for subsequent CO_2 conversion steps.

The performance and analysis reported herein promise practical potential for ocean-based carbon capture and utilization. So far, photoanode-photocathode device configuration operating in strong acid and base has shown ~ 20% solar-to-fuel conversion efficiency[34,35], and can be immediately applied to this flow PEC scheme for near neutral pH seawater. Our combined modeling and experiments suggest that the convective mass transfer compresses the consumption of dissolved inorganic carbon from seawater within a < 100-μm thin region. Thus, we can design multiple flow passes, employ high-surface-area photoelectrodes, and add convective mixing to effectively utilize seawater's ~ 2 mM carbon concentration. Furthermore, our reactor can draw inspiration from industrial tidal energy devices, reducing the energy consumption of flowing seawater and supplying seawater in real-time. For the capture and conversion of CO_2 using actual seawater in practice, it is necessary to pre-treat the seawater to prevent scaling and fouling. Our reactor currently produces a mixture of CO, CO_2, H_2, and O_2. If we separate O_2 through size sieving membranes and in real-time combine membrane separation[36] with flow photo-reactor, we can generate syngas, which undergo hydrogenation reactions for liquid fuel production[37,38].

Methods

Materials. Seawater salt was obtained from Instant Ocean. Vanadyl acetylacetonate ($VO(acac)_2$, 99.0%) and Bismuth nitrate pentahydrate ($Bi(NO_3)_3 \cdot 5H_2O$) are supplied by Millipore Sigma. Dimethyl sulfoxide (DMSO, AR) is obtained from Sigma-Aldrich. 18.25 MΩ cm ultra-pure water supplied by a Millipore system was used in the entire experimental process. All the reagents were used directly without further purification.

Characterization. The thickness of the a-Si on the polished Si (100) monitor substrate was obtained by a spectroscopic ellipsometer (M-2000 DI, J. A. Woollam Co., Inc.). The morphology and microstructure of the samples are characterized by field emission scanning electron microscope (FE-SEM, Hitachi S-8100, 5 kV). The UV-vis spectra are obtained on a SHIMADZU UV-2550 spectrophotometer. XPS measurements were performed using a PHI Versa Probe II Scanning XPS Microprobe equipped with a monochromatic Al source. The crystal structures were confirmed by XRD 271 using a Rigaku SmartLab X-ray Diffractometer in a grazing incident mode. Raman spectra were collected using a confocal Raman microscope (LabRAM HR Evolution, Horiba Jobin Yvon). The excitation source was a 532 nm laser. A 60X water-immersion objective (LUMPlanFL, Olympus) was used. For the in situ pH measurement, the Blue LED light with 415 nm single-wavelength light excitation (Item# M475L4h, FWHM = 17nm, Thorlabs) was used as the light source for $BiVO_4$ photoanode.

PEC measurements. PEC measurements were carried out using a three-electrode configuration with the prepared electrode as the working electrode, saturated Ag/AgCl as the reference electrode, and carbon as the counter electrode. The potentials obtained from each measurement were converted into values against the reversible hydrogen electrode using the Nernst equation: $E_{RHE}(V) = E_{Ag/AgCl} + 0.059 \times pH + 0.197$. A SP-300 Biologic potentiostat was used to control the potentials and record the data. The J-V curves of the samples were measured with a scan rate of 50 mV s^{-1} under irradiation with a 300 W Xenon lamp (Newport) equipped with an AM 1.5G filter. The gas products were analyzed by a gas chromatograph (Shimadzu, GC-8A) equipped with a thermal conductivity detector. Ar was used as a carrier gas.

Chlorine detection. After the stability test, the addition of 15 mL of 0.5 M KI (potassium iodide) to 10 mL of seawater would result in a color change if hypochlorite ions (ClO^-) are present. The reaction between ClO^- and iodide ions (I^-) would lead to the following color-indicative reaction: $ClO^- + 2I^- + 2H^+ = I_2 + Cl^- + H_2O$.

Fabrication of $BiVO_4$ photoanodes. $BiVO_4$ photoanodes were synthesized by metal organic decomposition methods, Bi and V precursors with 1 M dissolved DMSO simultaneously. Then, the precursors solution was filtered by a 0.45 μm pore size filter. After that, the precursors solution is deposited onto FTO by spin coating at 1000 rpm for 20 seconds followed by 3000 rpm for 40 seconds, calcined in a tube furnace at 500 ℃ (ramping rate of 5 ℃/min) for 2 h in the air. $NiFe(OH)_x$ catalyst with conformal coverage was deposited by citrate assisted method.

Fabrication of Si photocathodes, n^+-Si electrode, and Ag/Au/CrO_x. Czochralski (CZ) n-type Si substrates with a resistivity of 1–5 Ω cm, 155 μm thickness and (100)-orientation were used as the substrate. The silicon substrate was first textured using a mixture of potassium hydroxide and isopropyl alcohol, and then it was cleaned via standard RCA cleaning methods and finally dipped in 5% HF for 60 s to remove the surface native oxide layer. Followed by the cleaning process, the intrinsic a-Si passivation layers with 5 nm were deposited on both sides of Si by plasma enhanced chemical vapor deposition (PECVD). p^+-a-

Si and n^+-a-Si were deposited on the a-Si to enhance the driving force by constructing the heterojunction. After that, ITO layers were deposited on the highly doped a-Si layer as the current collect layer and anti-reflection layer. Ag paste with 20 μm thickness was scribbled on ITO layer by hand. 5 nm Au layer was deposited by magnetron sputtering. CrO_x was deposited onto Au layer by photoelectrochemical method, the potential was set to -0.2 V vs RHE, deposition time was 5 min. For the fabrication of Ag/Au/CrO_x dark electrode, the Ag, Au, and CrO_x were deposited onto the Ag plate.

The back contact of Si photocathode was made by connecting the copper tape with Ag paste. For n^+-Si electrode fabrication, the Ag paste was scribbled on the Si surface after HF treatment. The back contact of n^+-Si electrode was scratched by Indium/Gallium eutectic and connected with copper tape. When the connection was secured, it was further encapsulated by epoxy.

Fabrication of $BiVO_4$/Si tandem decives. The Indium was used to solder the back contact of $BiVO_4$ photoanode together with the Si photocathode to allow the charges to transfer to the ohmic back contact. Then, it was further encapsulated by epoxy.

Declarations

Acknowledgements

This research was funded by the Yale Planetary Solutions Project. S.H. gratefully acknowledges the financial support provided by the Division of Chemical Sciences, Geosciences and Biosciences, Office of Basic Energy Sciences, of the U.S. Department of Energy through an Early Career grant No. DE-SC0021953 for the photoelectrode development and interface characterizations. The authors thank Yuanzuo Gao (Yale University) for supporting the 3D printing efforts.

Author contributions

S. H supervised the project. S. H. and B. L. conceptualized the project. B. L., Z. Q, and X. S. developed the concept and carried out the experiments and data analysis. Catalyst synthesis procedures were developed and performed by H. S. and Y. Z., W. Z., A. K. and R. Y. contributed to the development of the photoelectrode fabrication method. All authors discussed the results and participated in the writing of the manuscript.

Competing interests

There are no conflicts to declare.

Additional information

Supplementary information. The online version contains supplementary materials.

Data availability

All data generated or analysed during this study are included in the published article and its Supplementary Information. Source data are provided with this paper.

Code availability

All codes used this study are provided upon request.

References

1. Zhu, P. *et al.* Continuous carbon capture in an electrochemical solid-electrolyte reactor. *Nature* **618**, 959-966 (2023). https://doi.org:10.1038/s41586-023-06060-1
2. Sharifian, R., Wagterveld, R. M., Digdaya, I. A., Xiang, C. & Vermaas, D. A. Electrochemical carbon dioxide capture to close the carbon cycle. *Energ Environ Sci* **14**, 781-814 (2021). https://doi.org:10.1039/D0EE03382K
3. Broström, G. The role of the annual cycles for the air-sea exchange of CO. *Marine Chemistry* **72**, 151-169 (2000). https://doi.org:Doi 10.1016/S0304-4203(00)00079-7
4. Yanagi, R. *et al.* Photocatalytic CO Reduction with Dissolved Carbonates and Near-Zero CO (aq) by Employing Long-Range Proton Transport. *Journal of the American Chemical Society* **145**, 15381-15392 (2023). https://doi.org:10.1021/jacs.3c03281
5. Digdaya, I. A. *et al.* A direct coupled electrochemical system for capture and conversion of CO(2) from oceanwater. *Nat Commun* **11**, 4412 (2020). https://doi.org:10.1038/s41467-020-18232-y
6. Eisaman, M. D. *et al.* CO2 extraction from seawater using bipolar membrane electrodialysis. *Energy & Environmental Science* **5** (2012). https://doi.org:10.1039/c2ee03393c
7. Kim, J. H., Hansora, D., Sharma, P., Jang, J. W. & Lee, J. S. Toward practical solar hydrogen production - an artificial photosynthetic leaf-to-farm challenge. *Chem Soc Rev* **48**, 1908-1971 (2019). https://doi.org:10.1039/c8cs00699g
8. Huang, D. *et al.* Over 1% Efficient Unbiased Stable Solar Water Splitting Based on a Sprayed Cu2ZnSnS4 Photocathode Protected by a HfO2 Photocorrosion-Resistant Film. *ACS Energy Letters* **3**, 1875-1881 (2018). https://doi.org:10.1021/acsenergylett.8b01005
9. Kobayashi, H. *et al.* Development of highly efficient CuIn0.5Ga0.5Se2-based photocathode and application to overall solar driven water splitting. *Energy & Environmental Science* **11**, 3003-3009 (2018). https://doi.org:10.1039/c8ee01783b
10. Xu, C. *et al.* Standalone Solar Carbon-Based Fuel Production Based on Semiconductors. *Cell Reports Physical Science* **1** (2020). https://doi.org:10.1016/j.xcrp.2020.100101
11. Liu, B. *et al.* Double-Side Si Photoelectrode Enabled by Chemical Passivation for Photoelectrochemical Hydrogen and Oxygen Evolution Reactions. *Advanced Functional Materials* **31** (2020). https://doi.org:10.1002/adfm.202007222
12. Liu, B. *et al.* Tandem cells for unbiased photoelectrochemical water splitting. *Chemical Society Reviews* **52**, 4644-4671 (2023). https://doi.org:10.1039/d3cs00145h

13. Wang, S. J. *et al.* An integrated n-Si/BiVO photoelectrode with an interfacial bi-layer for unassisted solar water splitting. *Chemical Science* **14**, 2192-2199 (2023). https://doi.org:10.1039/d2sc06651c
14. Tang, J. *et al.* Selective hydrogen peroxide conversion tailored by surface, interface, and device engineering. *Joule* **5**, 1432-1461 (2021). https://doi.org:https://doi.org/10.1016/j.joule.2021.04.012
15. Lees, E. W., Bui, J. C., Song, D., Weber, A. Z. & Berlinguette, C. P. Continuum Model to Define the Chemistry and Mass Transfer in a Bicarbonate Electrolyzer. *Acs Energy Lett* **7**, 834-842 (2022). https://doi.org:10.1021/acsenergylett.1c02522
16. Larrea, C., Torres, D., Avilés-Moreno, J. R. & Ocón, P. Multi-parameter study of CO2 electrochemical reduction from concentrated bicarbonate feed. *Journal of CO2 Utilization* **57** (2022). https://doi.org:10.1016/j.jcou.2021.101878
17. Zuddas, P. & Mucci, A. Kinetics of calcite precipitation from seawater: II. The influence of the ionic strength. *Geochim Cosmochim Ac* **62**, 757-766 (1998). https://doi.org:Doi 10.1016/S0016-7037(98)00026-X
18. Bai, S. *et al.* On factors of ions in seawater for CO2 reduction. *Applied Catalysis B: Environmental* **323** (2023). https://doi.org:10.1016/j.apcatb.2022.122166
19. Wang, Q. *et al.* Molecularly engineered photocatalyst sheet for scalable solar formate production from carbon dioxide and water. *Nature Energy* **5**, 703-710 (2020). https://doi.org:10.1038/s41560-020-0678-6
20. Li, C. *et al.* Photoelectrochemical CO2 reduction to adjustable syngas on grain-boundary-mediated a-Si/TiO2/Au photocathodes with low onset potentials. *Energy & Environmental Science* **12**, 923-928 (2019). https://doi.org:10.1039/c8ee02768d
21. Andrei, V. *et al.* Floating perovskite-BiVO(4) devices for scalable solar fuel production. *Nature* **608**, 518-522 (2022). https://doi.org:10.1038/s41586-022-04978-6
22. Wang, Q., Kalathil, S., Pornrungroj, C., Sahm, C. D. & Reisner, E. Bacteria-photocatalyst sheet for sustainable carbon dioxide utilization. *Nature Catalysis* **5**, 633-+ (2022). https://doi.org:10.1038/s41929-022-00817-z
23. Dunwell, M. *et al.* The Central Role of Bicarbonate in the Electrochemical Reduction of Carbon Dioxide on Gold. *Journal of the American Chemical Society* **139**, 3774-3783 (2017). https://doi.org:10.1021/jacs.6b13287
24. Zhang, Z., Xi, D. W., Ren, Z. C. & Li, J. A carbon-efficient bicarbonate electrolyzer. *Cell Reports Physical Science* **4** (2023).
25. Digdaya, I. A. *et al.* A direct coupled electrochemical system for capture and conversion of CO from oceanwater. *Nature Communications* **11** (2020).
26. Feng, S. J. *et al.* Enriched Surface Oxygen Vacancies of Photoanodes by Photoetching with Enhanced Charge Separation. *Angew Chem Int Edit* **59**, 2044-2048 (2020). https://doi.org:10.1002/anie.201913295
27. Li, M. *et al.* Zipping Up NiFe(OH)x-Encapsulated Hematite To Achieve an Ultralow Turn-On Potential for Water Oxidation. *ACS Energy Letters* **4**, 1983-1990 (2019).

https://doi.org:10.1021/acsenergylett.9b01430

28. Guo, J. *et al.* Direct seawater electrolysis by adjusting the local reaction environment of a catalyst. *Nature Energy* (2023). https://doi.org:10.1038/s41560-023-01195-x
29. Zhao, S. *et al.* Sputtered Stainless Steel on Silicon Photoanode for Stable Seawater Splitting in Photoelectrochemical Flow Cell. *Transactions of Tianjin University* **29**, 473-481 (2023). https://doi.org:10.1007/s12209-023-00374-x
30. Wang, K., Behdani, B. & Batista, C. A. S. Visualization of Concentration Gradients and Colloidal Dynamics under Electrodiffusiophoresis. *Langmuir* **38**, 5663-5673 (2022). https://doi.org:10.1021/acs.langmuir.2c00252
31. Kottmeier, D. M. *et al.* Reduced H channel activity disrupts pH homeostasis and calcification in coccolithophores at low ocean pH. *P Natl Acad Sci USA* **119** (2022).
32. Mehmood, A., Awais, M. & Dar, A. Generalized Pohlhausen integral method. *The European Physical Journal Plus* **139** (2024). https://doi.org:10.1140/epjp/s13360-023-04830-4
33. Li, T. *et al.* Electrolytic Conversion of Bicarbonate into CO in a Flow Cell. *Joule* **3**, 1487-1497 (2019). https://doi.org:https://doi.org/10.1016/j.joule.2019.05.021
34. Cheng, W.-H. *et al.* Monolithic Photoelectrochemical Device for Direct Water Splitting with 19% Efficiency. *ACS Energy Letters* **3**, 1795-1800 (2018). https://doi.org:10.1021/acsenergylett.8b00920
35. Fehr, A. M. K. *et al.* Integrated halide perovskite photoelectrochemical cells with solar-driven water-splitting efficiency of 20.8%. *Nature Communications* **14** (2023).
36. Ma, X. *et al.* Carbon monoxide separation: past, present and future. *Chem Soc Rev* **52**, 3741-3777 (2023). https://doi.org:10.1039/d3cs00147d
37. Li, X. *et al.* Fast-Response Nickel-Promoted Indium Oxide Catalysts for Carbon Dioxide Hydrogenation from Intermittent Solar Hydrogen. *Angew Chem Int Ed Engl* **62**, e202301901 (2023). https://doi.org:10.1002/anie.202301901
38. He, Y. *et al.* Significant Roles of Surface Hydrides in Enhancing the Performance of Cu/BaTiO(2.8) H(0.2) Catalyst for CO(2) Hydrogenation to Methanol. *Angew Chem Int Ed Engl* **63**, e202313389 (2024). https://doi.org:10.1002/anie.202313389

Figures

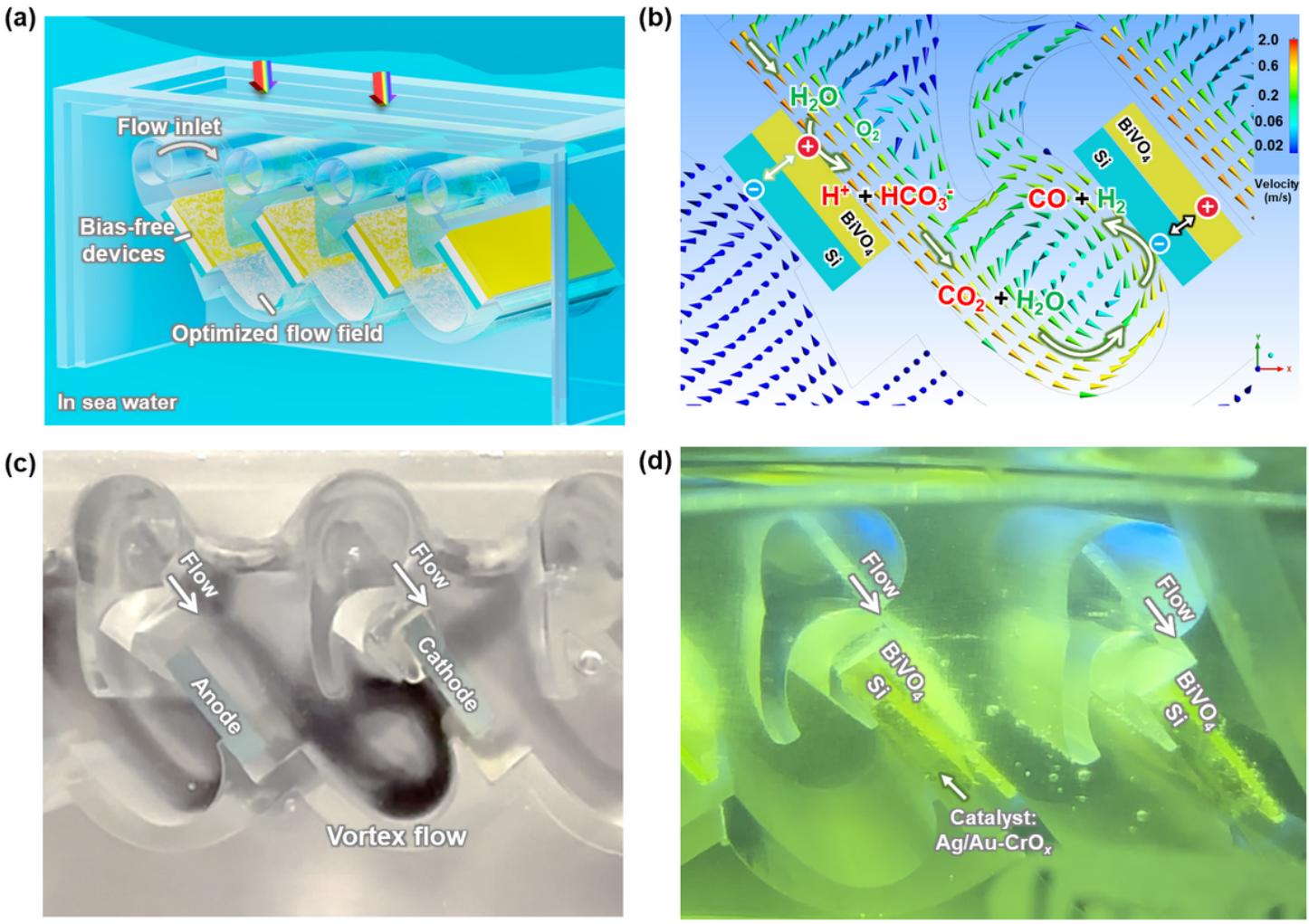

Figure 1

Ocean reactor with enhanced flow field for CO_2 extraction and in-situ utilization in seawater. a, The schematic illustration of in-situ generated CO_2 in a floating reactor in seawater. b, The flow field simulation. c, the vortex flow pattern which is highlighted by black ink. d, Photograph of CO_2 capture and in-situ conversion in seawater under 1 sun AM 1.5G.

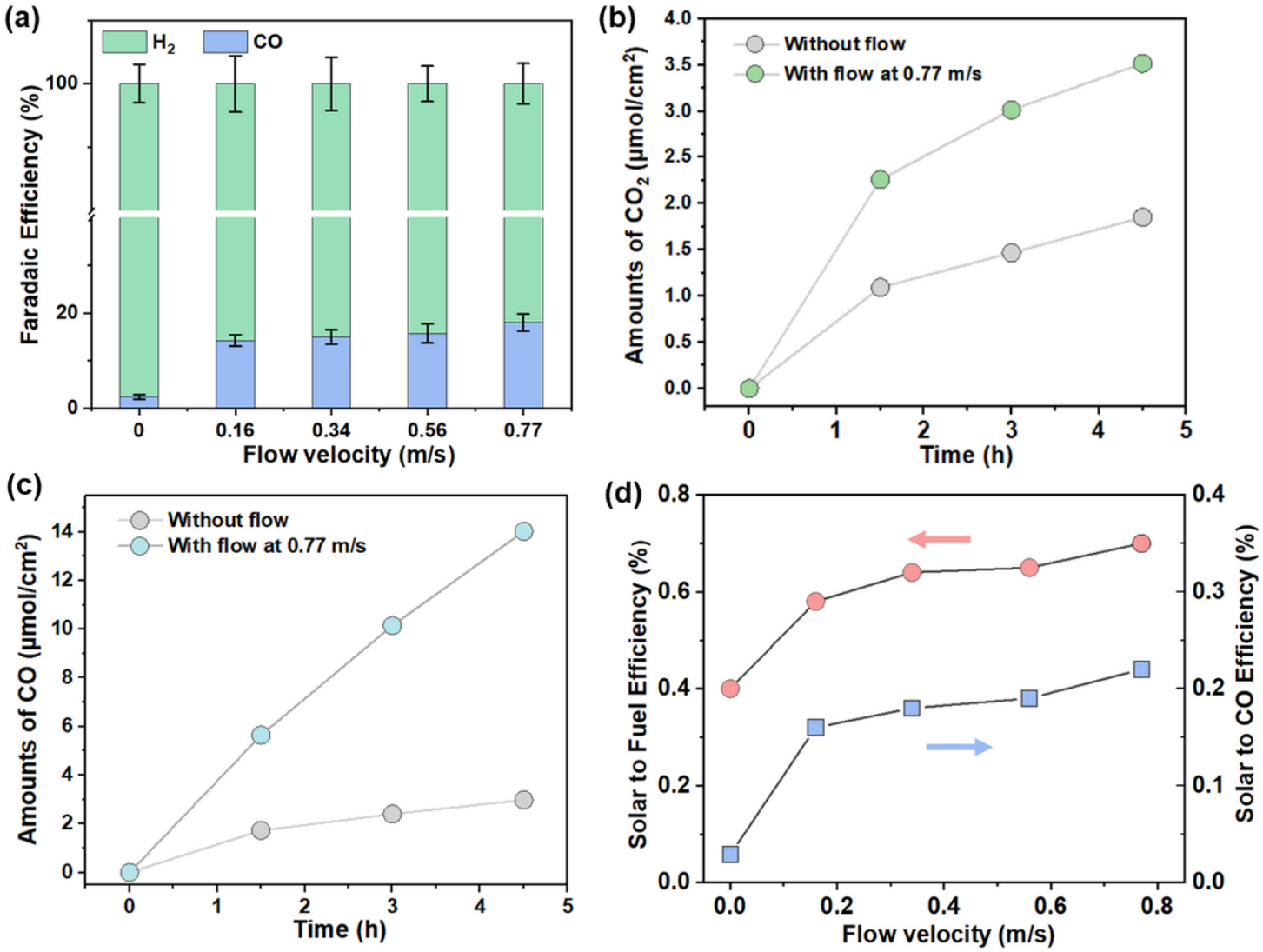

Figure 2

Flow velocity dependent performance and activity for CO_2 extraction and in-situ utilization in seawater. a, The Faradaic efficiencies of CO and H_2 at various flow velocities. The error bars represent the standard deviations of three independent measurements of the same samples. b, Time course of CO_2 gas production. c, Time course of CO gas production. d, Solar-to-Fuel and solar-to-CO efficiencies at different seawater flow velocities measured at 0.3 cm above the surface of the $BiVO_4$ photoanode near the inlet.

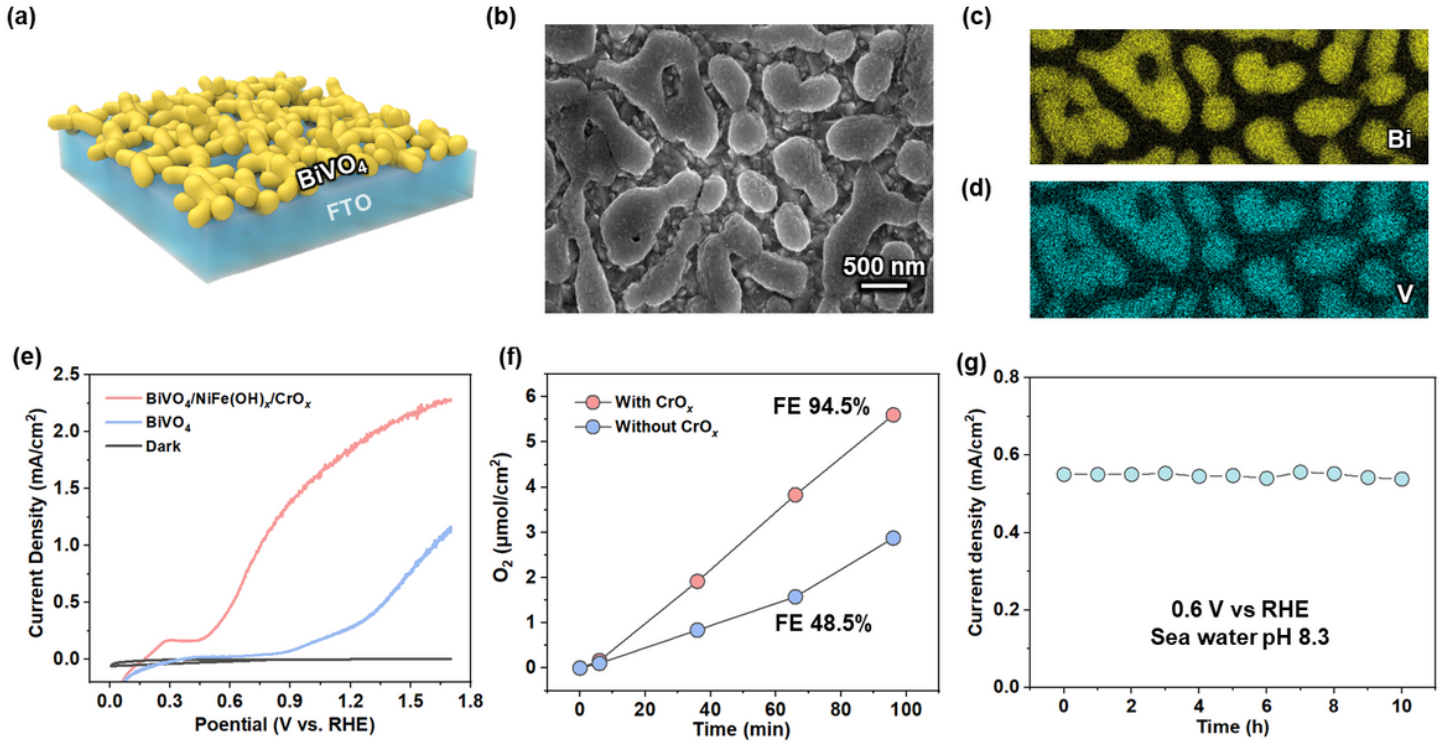

Figure 3

$BiVO_4$ photoanodes for seawater oxidation. a, The schematics of $BiVO_4$ photoanodes. b, The scanning electron microscopy image, and corresponding element mapping of Bi (c) and V (d). e, *J-E* curves of $BiVO_4$ photoanode with or without catalysts under illumination and in the dark. f, Time course of O_2 gas production. g, Stability of $BiVO_4$ photoanode at 0.6 V vs RHE.

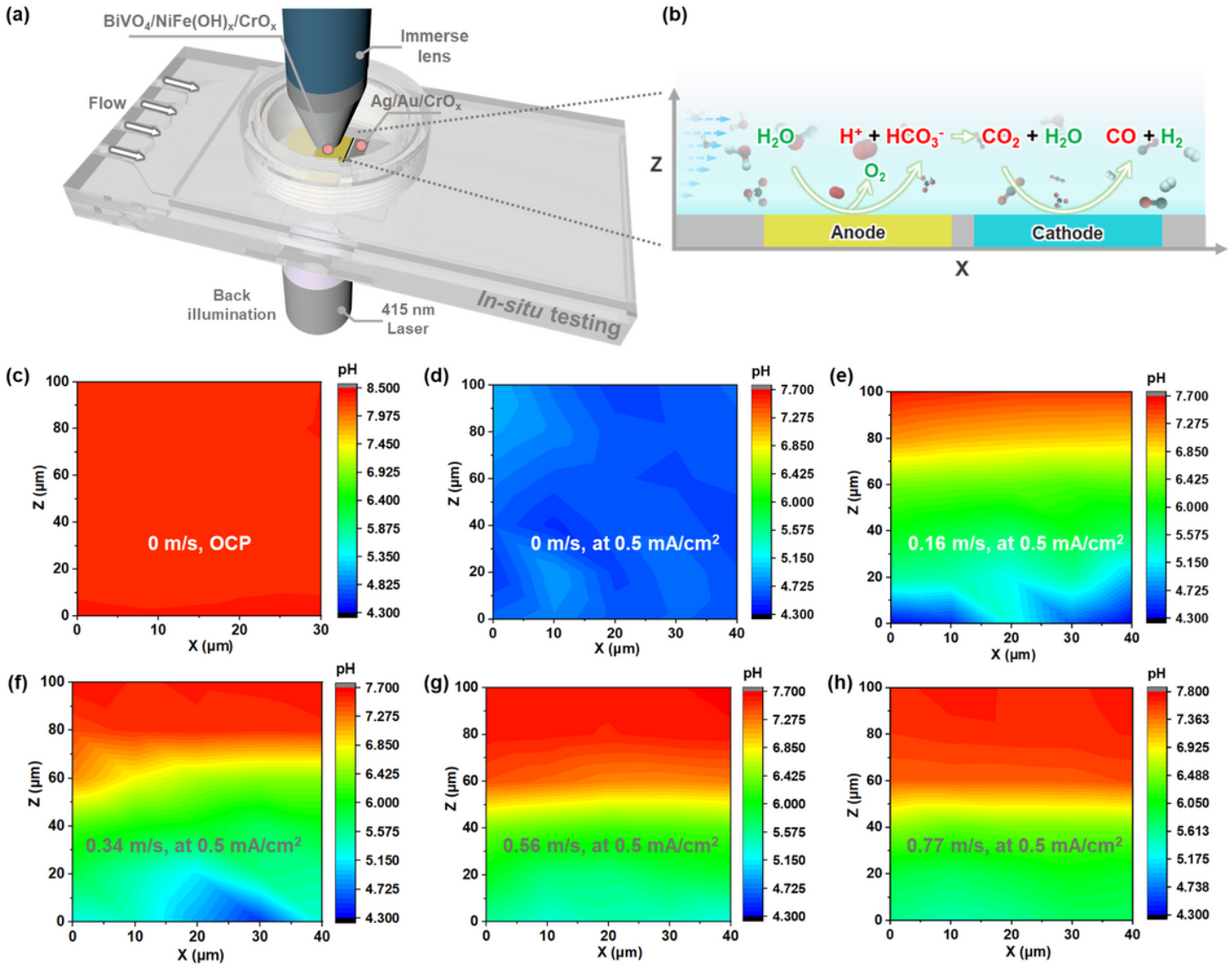

Figure 4

In-situ pH measurement on $BiVO_4$ photoanode for water oxidation. a, The schematics of in situ Raman set-up for pH measurement. b, The zoom-in illustration of water oxidation and CO_2 reduction reaction during *in-situ* Raman measurement. The data collected at x=0.8cm at the anode along the length of the anode. c, pH profile on $BiVO_4$ photoanode under OCP. pH profiles on $BiVO_4$ photoanode at 0.5 mA/cm^2 under flow velocities of 0 (d), 0.16 (e), 0.34 (f), 0.56 (g), and 0.77 m/s (h).

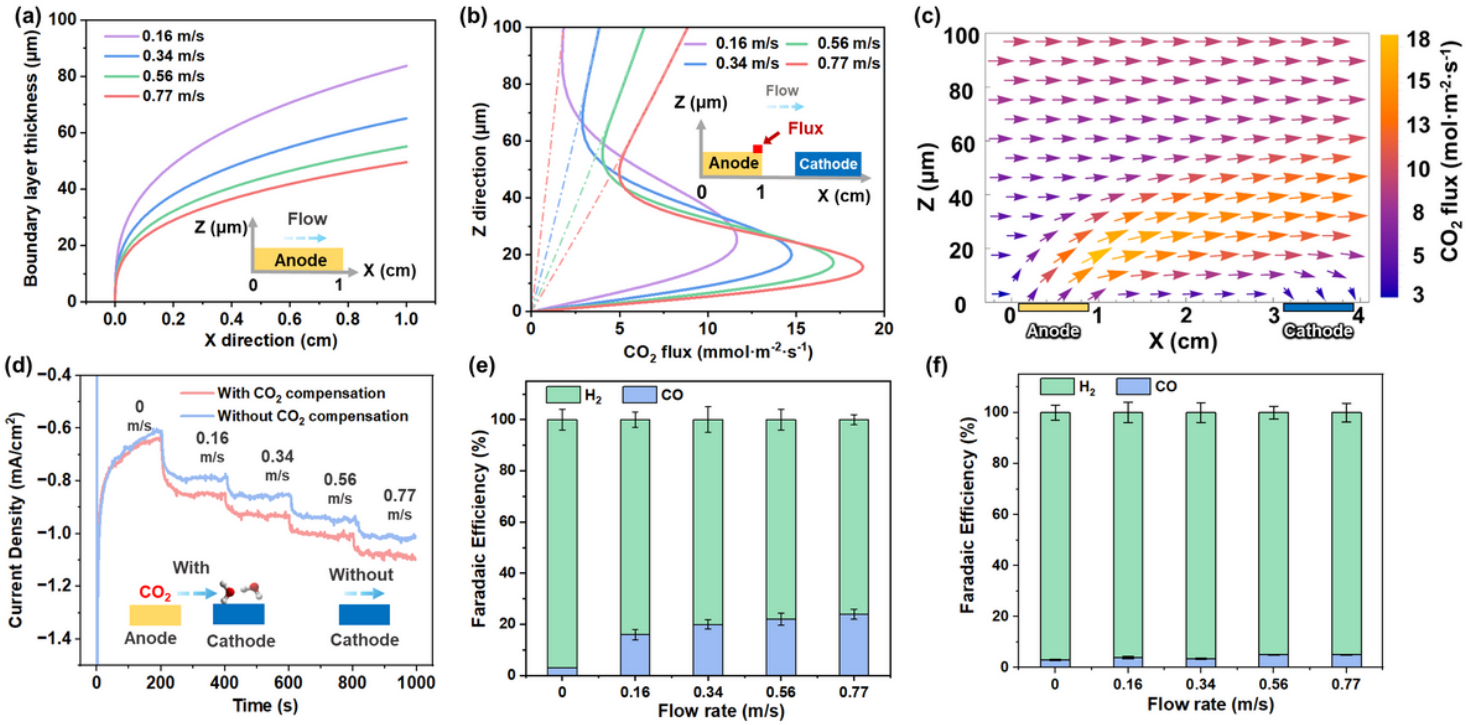

Figure 5

Convective mass transfer flux calculation and experimental validation for CO_2 capture and conversion. a, the calculated boundary layer thickness of anode at different flow velocity, u_0 and flow distance x_0, labeled as X-axis. b, convective flux of CO_2 at the end of anode (X = 1 cm) at different flow rates; c, vector flux profile of CO_2 at 0.77 m/s. d, flow rate dependent current density with and without CO_2 compensation at -0.5 V vs RHE. (e) Faradaic efficiency of CO and H_2 at different flow rates with CO_2 compensation. (f) Faradaic efficiency of CO and H_2 at different flow rates without CO_2 compensation. The current density applied in (a-c) was 0.5 mA/cm^2. The voltage applied in (d-f) was -0.5 V vs RHE

Supplementary Files

This is a list of supplementary files associated with this preprint. Click to download.

- Video.mp4
- SiBVOSIsubmission.docx